Article

TiO$_2$ Catalysts Co-Modified with Bi, F, SnO$_2$, and SiO$_2$ for Photocatalytic Degradation of Rhodamine B Under Simulated Sunlight

Lu Qiu [1], Hanliang Li [2], Wenyi Xu [3], Rongshu Zhu [3,]* and Feng Ouyang [3,]*

1   College of Eco-Environmental Engineering, Guizhou Minzu University, Guiyang 550025, China;
    202001089@gzmu.edu.cn
2   Environmental Science and Engineering Department, Liaoning Technical University, Fuxin 123000, China;
    lihanliang2012@126.com
3   Shenzhen Key Laboratory of Organic Pollution Prevention and Control, Harbin Institute of Technology,
    Shenzhen 518055, China
*   Correspondence: rszhu@hit.edu.cn (R.Z.); ouyangfh@hit.edu.cn (F.O.)

Abstract: The organic pollutants discharged from industrial wastewater have caused serious harm to human health. The efficient photocatalytic degradation of organic pollutants under sunlight shows promise for industrial applications and energy utilization. In this study, a modified TiO$_2$ photocatalyst doped with bismuth (Bi) and fluorine (F) and composited with SnO$_2$ and SiO$_2$ was prepared, and its performance for the degradation of Rhodamine B (RhB) under simulated sunlight was evaluated. Through the optimization of the doping levels of Bi and F, as well as the ratio of SnO$_2$ and SiO$_2$ to TiO$_2$, the optimal catalyst reached degradation efficiency of 100% for RhB within 20 min under simulated sunlight, with a first-order reaction rate constant of 0.291 min^{-1}. This value was 15, 41, 6.5, and 3.3 times higher than those of TiO$_2$/SnO$_2$, Bi/TiO$_2$, Bi-TiO$_2$/SnO$_2$, and F/Bi-TiO$_2$/SnO$_2$, respectively. The active species detection showed that h$^+$ was the most crucial active species in the process. The role of Bi and F addition and SnO$_2$-SiO$_2$ compositing was investigated by characterization. Bi formed a chemical bonding with TiO$_2$ by doping into TiO$_2$. The absorbance intensity in the UV and visible light regions was improved by SnO$_2$ and F modification. Composite with SiO$_2$ led to a larger surface area that allowed for more RhB adsorption sites. These beneficial modifications greatly enhanced the photocatalytic activity of the catalyst.

Keywords: photocatalysis; TiO$_2$; bismuth; SnO$_2$; rhodamine B; organic pollutant removal

1. Introduction

Industrial wastewater discharge always introduces organic pollutants, such as dyes, herbicides, pesticides, analgesics, and antibiotics into the water environment, causing serious water problems and posing severe threats to the ecosystem and human health. Photocatalytic treatment is an advanced oxidation process (AOP) that is promising, economical, efficient, and sustainable for degrading organic pollutants in water using solar energy. It is well known that titanium dioxide (TiO$_2$) has long been one of the most widely researched and applied semiconductor materials in the field of photocatalysis due to its suitable band structure, low cost, non-toxicity, and high stability [1,2]. However, the wide bandgap of TiO$_2$ (3.0–3.2 eV) limits its spectral response only in the ultraviolet region. Another disadvantage is its rapid recombination of photoelectrons and holes [3,4]. These defects limit its practical efficiency in the photocatalytic degradation of organic pollutants under sunlight. To overcome this disadvantage, researchers have explored various strategies, such as doping with metals and non-metals [5–7], loading co-catalysts [8,9], designing heterojunctions [10,11], and adjusting morphology [12,13]. By modulating TiO$_2$ properties from different perspectives, these endeavors are intended to enhance its absorption and

utilization of light, restrain photo-generated carrier recombination, and ultimately improve photocatalytic efficiency.

Doping TiO_2 with metals or non-metals is a well-established method for boosting its photocatalytic activity. Research on non-metal doping always includes C, S, N, B, and F dopants. Among these, fluorine doping has been demonstrated to enhance catalytic activity of TiO_2 in organic pollutant degradation, possibly by inducing the formation of surface oxygen vacancies [14,15] and Ti^{3+} defects [16] or increasing surface hydroxyl groups [17,18]. In addition, there are many kinds of doped metals. The addition of impurities in the pure semiconductor proves effective in generating electron–hole traps and narrowing the bandgap [19], thereby improving photocatalytic efficiency. Among these doped metals, bismuth has been used as a dopant effectively. Bi_2O_3 is a common Bi (III)-based compound with a suitable bandgap width (2.3–2.8 eV) [20,21]. Bi_2O_3 and TiO_2 exhibit matched band structures. It has been proved that doped Bi can reduce the bandgap and promote the separation of photo-generated carriers [22–24]. The bandgap reduction resulted from the up-shift valence band that was triggered by the hybridization of Bi (6 s) orbital with O (2p) orbital [25]. Research studies have pointed out that the modification of various forms of TiO_2 with Bi_2O_3 enhanced its visible light catalytic activity against certain organic dyes [26,27]. Additionally, coupling TiO_2 with other semiconductors to form photocatalytic heterojunctions is a strategy to facilitate the separation of photo-generated carriers. Tin dioxide (SnO_2), an ideal and typical oxide semiconductor material with a bandgap of 3.6 eV, shares certain similarities with TiO_2 in terms of the crystal structure [28], making it conducive to constructing heterojunction structures [29,30]. Tin modification of TiO_2 can reduce the binding of photo-generated electron–hole pairs, thus facilitating the degradation of complex pollutants [31,32]. It was reported that the forming of $Ti_{1-x}Sn_xO_2$ solid solutions generated type II heterojunctions [32], which achieved effective charge separation. Moreover, the formation of TiO_2-SnO_2 composite aids in the reduction in the bandgap, which shifts the optical absorption from UV to the visible region [33,34]. The effective charge separation was achieved by promoting the holes (h^+) to the lower valence band (VB) of TiO_2 and the electrons (e^-) to the lower conduction band (CB) of SnO_2 [35–38]. For these reasons, the SnO_2-TiO_2 composite showed improved activity in the photocatalytic degradation of organic pollutants under visible light [39–41].

Moreover, the diminutive specific surface area of TiO_2 leads to limited adsorption capacity and a small number of activity sites for the reactants [42,43]. Therefore, to improve the adsorption ability of TiO_2 towards organic pollutants, combining TiO_2 with other materials with a large surface area serves as a promising approach to achieve this target [44–47].

To sum up, numerous methods and diverse added chemical compounds have been explored for modifying TiO_2 to enhance its photocatalytic performance. Therefore, a combination of co-doping and compositing holds theoretical feasibility in comprehensively improving properties of TiO_2, such as absorption of ultraviolet and visible light, separation of photo-generated carrier, high surface area, etc., and in further bolstering the degradation efficiency of organic pollutants under simulated sunlight. Up to now, F, Bi, or Sn modification has been reported to enhance the performance of TiO_2. However, the co-doping of F and Bi, along with SnO_2 and SiO_2 compositing, to synthesized TiO_2 has not been reported to our knowledge. The TiO_2 catalyst modified by F-Bi-Sn-Si was synthesized for the first time, and its performance on RhB degradation was investigated in terms of optical properties.

Herein, this study employed homogeneous precipitation and sol–gel methods to synthesize F/Bi-$TiO_2/SnO_2/SiO_2$ photocatalysts. These materials were utilized for the photocatalytic degradation of RhB under simulated solar light. Various techniques were employed to characterize the optical and physicochemical properties, with an aim to elucidate the impact of different element doping or compositing on catalyst structure and properties. Given the enhanced performance of the prepared catalysts, the efficient degradation of RhB was achieved under simulated solar light.

2. Results

2.1. Impact of Bi Addition and Compositing with SnO₂ on Catalyst Properties

2.1.1. Impact on Crystal Phase

To analyze the influence of Bi and SnO_2 modification on the crystal phase, X-ray diffraction (XRD) patterns of Bi-TiO_2/SnO_2 catalysts with different Bi doping amounts and different SnO_2/TiO_2 molar ratios were assessed. Figure 1A shows the XRD spectra of Bi-TiO_2/SnO_2 catalysts with varying Bi amounts. All catalysts exhibited diffraction peaks at 25.3°, 37.9°, and 48.0°, corresponding to (101), (004), and (200) crystal faces of anatase TiO_2 (JCPDS 21–1272), while other weak diffraction peaks were assigned to rutile TiO_2. The peaks at 26.81°, 34.31°, and 54.18° corresponded to (110), (101), and (211) crystal faces of rutile SnO_2. The results indicated the existence of TiO_2 and SnO_2 primarily in the forms of anatase and rutile phases, respectively. No diffraction peaks of Bi oxides were observed in the XRD patterns, suggesting that no crystalline Bi oxides were formed. This could be attributed to Bi being doped into the TiO_2 lattice in the ionic form or being highly dispersed [24,48,49]. The crystal grain size was calculated and listed in Table S1. Although no Bi diffraction peaks were present, the crystal grain size showed varying degrees of decrease with the addition of Bi, indicating that Bi doping reduced the crystal grain size of TiO_2 [24,50]. Figure 1B illustrates the influence of the SnO_2/TiO_2 molar ratio on the XRD spectra of Bi-TiO_2/SnO_2 catalysts. All catalysts exhibited characteristic peaks of anatase TiO_2 and rutile SnO_2. Different Sn/Ti molar ratios did not cause a change in the crystal form, indicating that the addition of SnO_2 did not alter the TiO_2 crystal phase.
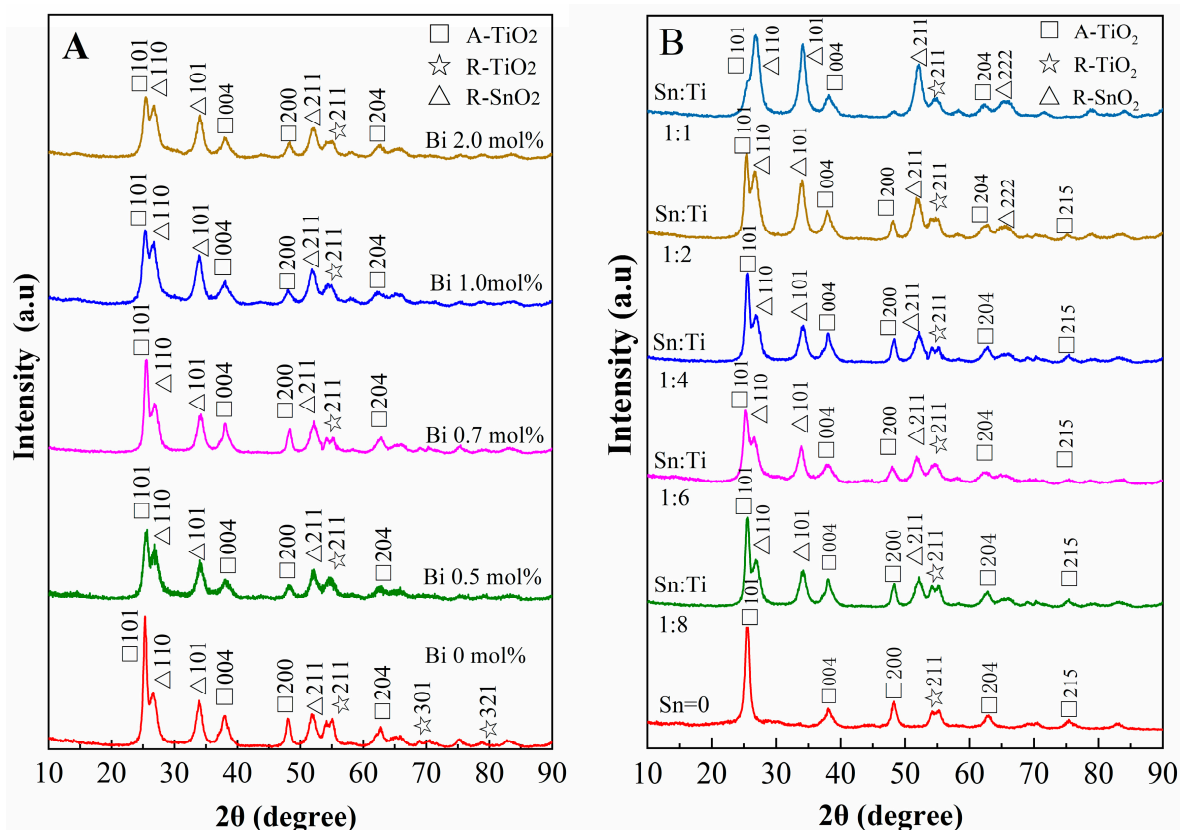

Figure 1. XRD patterns of Bi-TiO_2/SnO_2 samples with (**A**) different Bi amounts and (**B**) different SnO_2/TiO_2 molar ratios.

2.1.2. X-Ray Photoelectron Spectroscopy Analysis

The X-ray photoelectron spectroscopy (XPS) was introduced to evaluate the surface chemical and elemental states of the Bi-TiO_2/SnO_2 catalyst. Figure 2A presents the Ti 2p spectrum of Bi-TiO_2/SnO_2, with distinct Ti $2p_{3/2}$ and Ti $2p_{1/2}$ peaks appearing at 458.72 eV

and 464.38 eV, respectively. These peaks exhibited a slight shift towards higher values compared to the standard features of TiO_2 (458.6 eV and 464.3 eV), indicating that Ti in the sample was in a combined state with Bi [49]. The O 1s spectrum of Bi-TiO_2/SnO_2 in Figure 2B could be decomposed into two peaks, with one binding energy at 530.28 eV, between the O 1s standard binding energies of TiO_2 and SnO_2 (530.08 eV and 530.94 eV), indicating lattice oxygen [51]. The other peak at 532.02 eV was assigned to surface hydroxyl oxygen [52]. Figure 2C exhibits the Bi 4f spectrum of the Bi-TiO_2/SnO_2 catalyst. The binding energy values of Bi $4f_{7/2}$ and Bi $4f_{5/2}$ were 159.23 eV and 164.18 eV, respectively. However, according to the binding energy handbook, the XPS peak positions for Bi^{3+} in Bi $4f_{7/2}$ and Bi $4f_{5/2}$ are 158.5 eV and 162.2 eV, respectively. Therefore, it indicated that, due to electron transfer interactions with TiO_2, Bi existed in a higher-valence $Bi^{3+\sigma}$ state, which formed a certain type of chemical bonding with TiO_2 [53]. Combined with the previous XRD result that Bi entered into the TiO_2 lattice, the $Bi^{3+\sigma}$ occupation in the catalyst lattice could cause lattice distortion. To compensate for the energy change triggered by lattice distortion, more oxygen vacancies were generated on the catalyst, acting as traps for photo-generated electrons and hindering their recombination with holes, ultimately elevating the efficiency of the photocatalytic reaction. On the other hand, the hybridization of Bi with O orbital could form hybrid energy [25]. Figure 2D shows the high-resolution spectrum of Sn 3d for Bi-TiO_2/SnO_2 catalysts. The Sn $3d_{5/2}$ peak appeared at 486.51 eV and the Sn $3d_{3/2}$ peak at 494.88 eV, with a separation of 8.37 eV, illustrating that tin existed as Sn (IV) [28,54]. The full survey spectrum for the Bi-TiO_2/SnO_2 sample is depicted in Figure 2E.
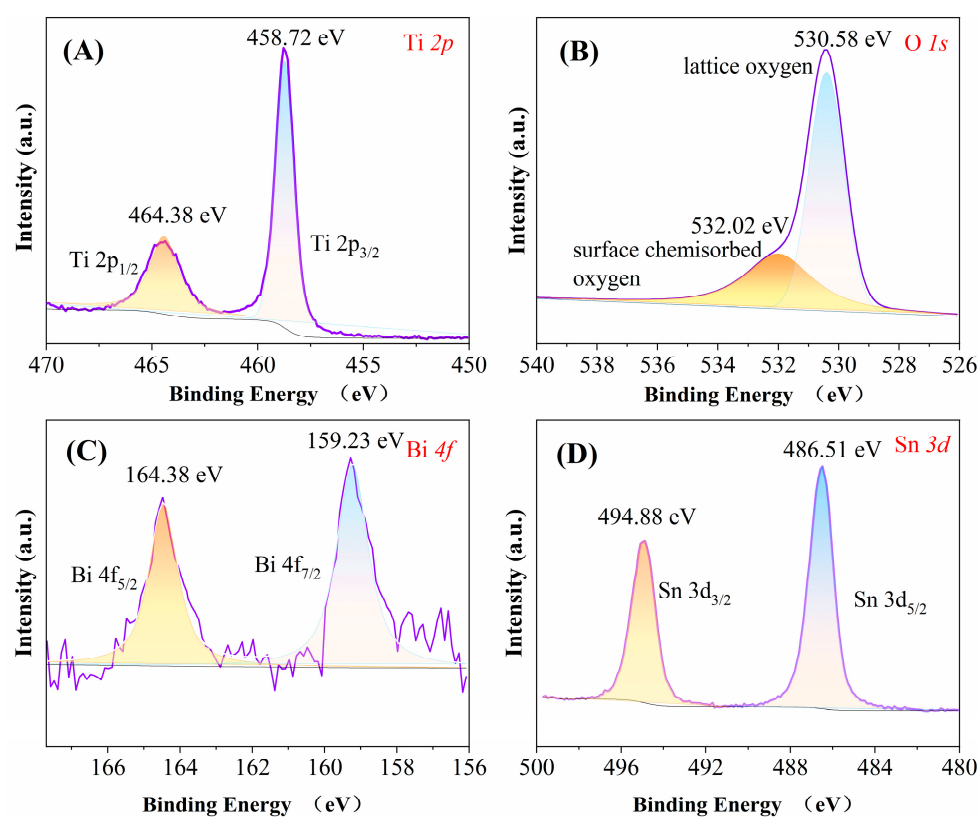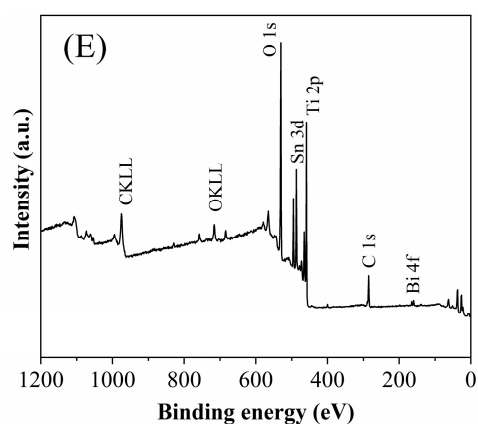

Figure 2. *Cont.*

Figure 2. High-resolution XPS spectra of the as-prepared Bi-TiO$_2$/SnO$_2$ of (**A**) Ti 2p, (**B**) O 1s, (**C**) Bi 4f, (**D**) Sn 3d, and (**E**) the overall XPS spectrum.

2.1.3. Impact on Surface Morphology

To analyze the influence of Bi and SnO$_2$ addition on the surface morphology of the catalyst, scanning electron microscopy (SEM) was performed for TiO$_2$/SnO$_2$, Bi-TiO$_2$/SnO$_2$, and Bi-TiO$_2$. Figure 3A presents the SEM image of TiO$_2$/SnO$_2$. It can be seen that, without Bi addition, the TiO$_2$/SnO$_2$ exhibited a dense and smooth surface of the primary particles. Figure 3C presents that Bi doping induced a loose and porous structure on the catalyst's surface, indicating that the addition of Bi promoted the dispersion of particles, possibly due to the inhibiting effect of Bi doping during the formation of TiO$_2$ crystals, which is consistent with the XRD results. Comparing Figure 3B with Figure 3C, the results showed that the addition of SnO$_2$ had no obvious effect on the surface morphology from the SEM images.
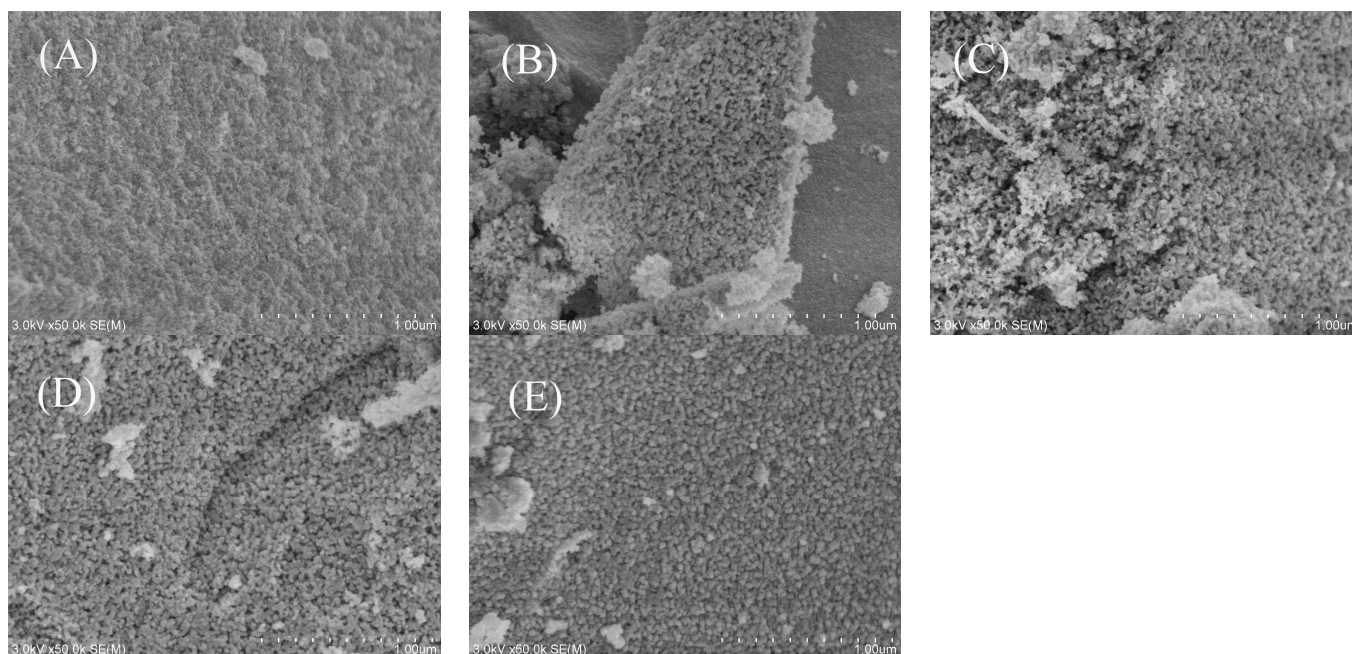

Figure 3. SEM images of (**A**) TiO$_2$/SnO$_2$; (**B**) Bi-TiO$_2$; (**C**) Bi-TiO$_2$/SnO$_2$; (**D**) F-Bi-TiO$_2$/SnO$_2$; and (**E**) F-Bi-TiO$_2$/SnO$_2$/SiO$_2$.

2.1.4. Impact on Optical Properties

Figure 4A displays the UV–vis diffuse reflectance spectra (DRSs) of TiO$_2$/SnO$_2$, Bi-TiO$_2$, and Bi-TiO$_2$/SnO$_2$. It can be seen that, compared to TiO$_2$/SnO$_2$, Bi-TiO$_2$/SnO$_2$ exhibited stronger absorbance in UV light regions but weaker absorbance in visible light

regions, indicating improved UV light-harvesting properties due to Bi doping. Compared to Bi-TiO$_2$, Bi-TiO$_2$/SnO$_2$ showed enhanced absorbance in both the UV and visible light regions. It indicated that the combination with SnO$_2$ can improve the absorption of visible and ultraviolet light. The bandgaps were calculated by Tauc plot based on DRS results (Figure 4B), and the bandgap energies (E_g) of Bi-TiO$_2$, TiO$_2$/SnO$_2$, and Bi-TiO$_2$/SnO$_2$ were 3.00, 2.94, and 2.97 eV, respectively. This calculated result showed that the Bi and SnO$_2$ modifications have no significant effects on the bandgap.
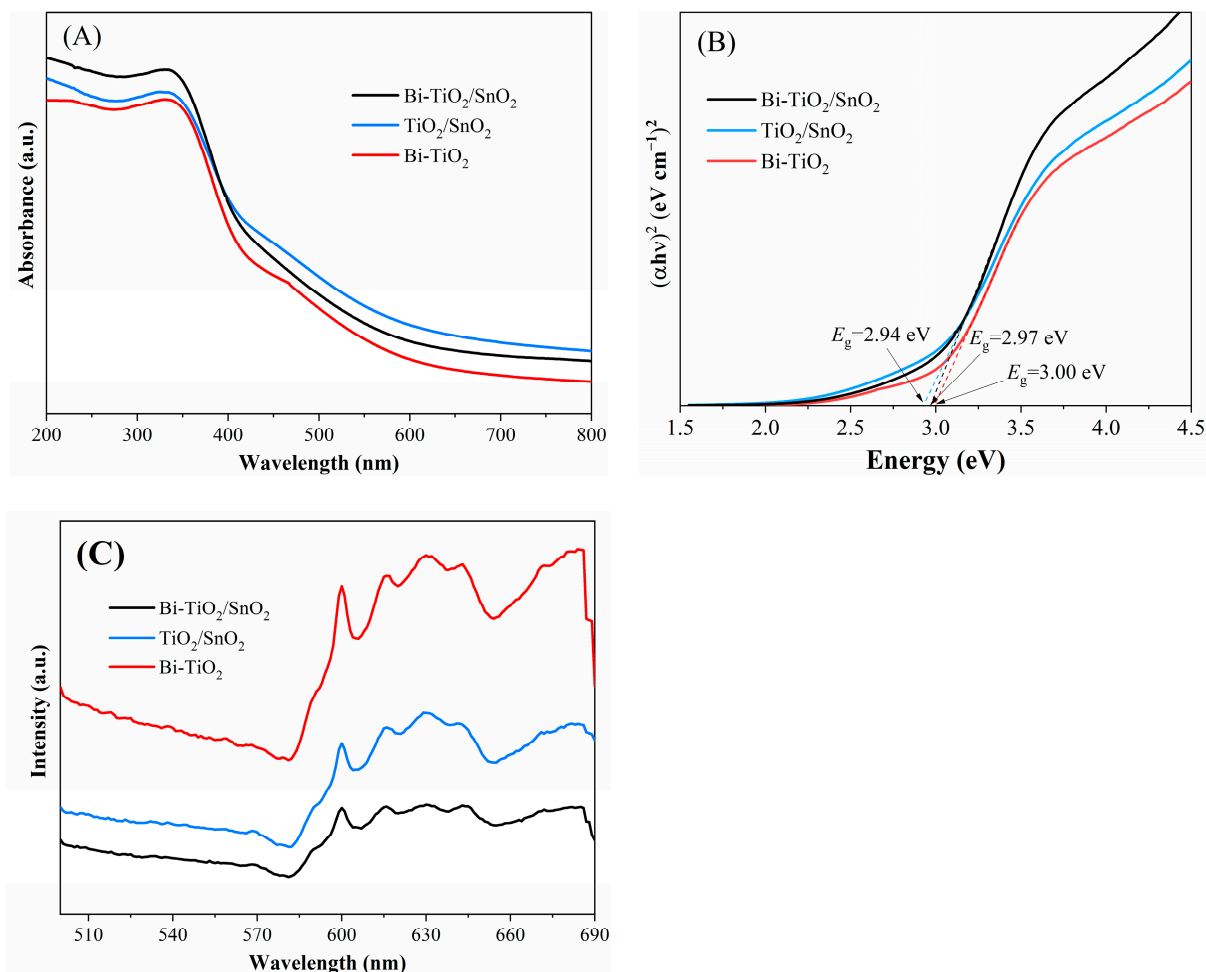

Figure 4. (**A**) UV–vis DRS of TiO$_2$/SnO$_2$, Bi-TiO$_2$, Bi-TiO$_2$/SnO$_2$; (**B**) the corresponding Tauc plot; and (**C**) the corresponding photoluminescence spectra.

Figure 4C shows the photoluminescence (PL) spectra of TiO$_2$/SnO$_2$, Bi-TiO$_2$, and Bi-TiO$_2$/SnO$_2$. The PL spectra are related to the transfer behavior of photo-generated carriers. A higher PL intensity indicates a higher recombination rate of photo-generated carriers [55]. As shown in Figure 4C, the PL spectrum of Bi-TiO$_2$/SnO$_2$ did not exhibit new emission peaks compared to TiO$_2$/SnO$_2$ and Bi-TiO$_2$, indicating that Bi doping and SnO$_2$ composite did not induce new emission phenomena. Compared to TiO$_2$/SnO$_2$, Bi-TiO$_2$/SnO$_2$ had relatively weak emission intensity, indicating that a certain amount of Bi doping inhibited the recombination of photo-generated carriers. Coupled with the XRD and XPS results, the reason could be that Bi doping triggers lattice distortion, generating impurity levels and more oxygen vacancies that serve as traps for photo-generated electrons. Compared to Bi-TiO$_2$, Bi-TiO$_2$/SnO$_2$ exhibited a significantly reduced PL intensity, indicating that the appropriate amounts of SnO$_2$ can enhance the separation of photo-generated carriers. This may be attributed to the transfer of photo-generated electrons from CB of TiO$_2$ to SnO$_2$ and

the movement of holes from VB of SnO_2 to TiO_2, which improve the separation efficiency of photon-generated carriers [38].

2.2. Impact of Bi and SnO_2 Addition on RhB Photocatalytic Degradation

　　　The influence of Bi amounts and the molar ratio of SnO_2 to TiO_2 on the photocatalytic activity of Bi-TiO_2/SnO_2 under simulated sunlight were investigated. Figure 5A shows the RhB degradation curves of Bi-TiO_2/SnO_2 prepared with varying Bi amounts. The degradation efficiency initially increased and then decreased with increasing Bi doping. The catalyst exhibited the highest activity when the Bi doping level was 0.7 mol%, achieving an RhB degradation rate of 96.56% after 60 min of reaction. Beyond the doping level of 0.7 mol%, the catalytic activity decreased. The reason may be that a moderate amount of Bi is an effective charge separator, but beyond a certain amount, it begins to act as a new recombination center [50].
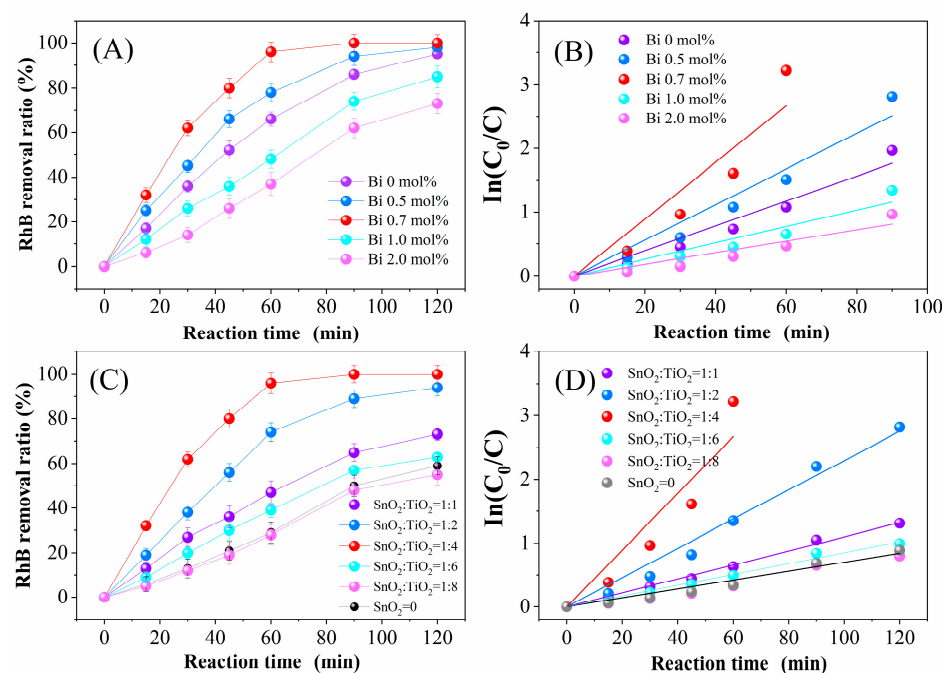

Figure 5. (**A**) Photocatalytic removal curves and (**B**) pseudo-first-order kinetics curves for the degradation of RhB by Bi-TiO_2/SnO_2 with different Bi amounts; (**C**) photocatalytic removal curves and (**D**) pseudo-first-order kinetics curves of Bi-TiO_2/SnO_2 with different SnO_2/TiO_2 molar ratios.

　　　Figure 5C illustrates the degradation curves of Bi-TiO_2/SnO_2 catalysts with different SnO_2/TiO_2 molar ratios. With an increasing SnO_2 proportion, the degradation efficiency of RhB initially increased and then decreased. The optimum catalytic activity was observed at a SnO_2/TiO_2 molar ratio of 1:4, indicating that the composite of TiO_2 with SnO_2 in a specific ratio is advantageous for boosting the photocatalytic activity.

　　　The activity test results suggested that the optimal Bi doping amount was 0.7 mol%, and the optimal SnO_2:TiO_2 molar ratio was 1:4. The RhB degradation processes were fitted by the pseudo-first-order model (Figure 5B,D). The results showed that the optimized Bi-TiO_2/SnO_2 had a reaction rate constant (*k*) of 0.0621 min^{-1}. This value was 6.4 times that of the Bi-TiO_2 catalyst and 2.3 times that of the TiO_2/SnO_2 catalyst (Figure S2). It indicated that the addition of Bi and the combination with SnO_2 significantly boosted the catalyst's activity, which was consistent with the improvements in light absorption performance observed through DRS and PL.

2.3. Impact of F Addition and Compositing with SiO$_2$ on Catalyst Properties

2.3.1. Surface Morphology

The effect of F addition and compositing with SiO$_2$ on the surface morphology of the catalyst was analyzed by SEM. Figure 3C–E show the surface morphology images of Bi-TiO$_2$/SnO$_2$, F/Bi-TiO$_2$/SnO$_2$, and F/Bi-TiO$_2$/SnO$_2$/SiO$_2$. It can be observed that all three catalysts consist of primary particles with relatively uniform sizes that aggregate into amorphous secondary particles. Comparing Figures 3C and 3D, the F addition made the catalyst particles more uniformly dispersed, with numerous tiny grains scattered on the surface, inhibiting particle aggregation. This was speculated to be caused by the etching effect of hydrofluoric acid on the sample surface [56]. Comparing Figures 5C and 3E, compositing with SiO$_2$ led to a more uniform distribution of the particles, with a smoother surface. It was inferred that, due to the porous structure of SiO$_2$ [57], catalytic active sites were evenly distributed on the catalyst surface while suppressing grain growth and aggregation.

2.3.2. Crystal Phase

To understand the impact of F and SiO$_2$ addition on the crystal phase of the catalyst, XRD characterization was performed on Bi-TiO$_2$/SnO$_2$, F/Bi-TiO$_2$/SnO$_2$, and F/Bi-TiO$_2$/SnO$_2$/SiO$_2$ (Figure 6). Comparing the spectra of Bi-TiO$_2$/SnO$_2$ and F/Bi-TiO$_2$/SnO$_2$ revealed that F addition resulted in finer and higher TiO$_2$ diffraction peaks. The crystal grain size calculated in Table S1 indicated that F modification restrained the growth of TiO$_2$ grains [58]. In fact, F was mostly doped into the TiO$_2$ lattice, which was demonstrated by the XPS characterization of F-Bi-TiO$_2$/SnO$_2$ (Figure S3).
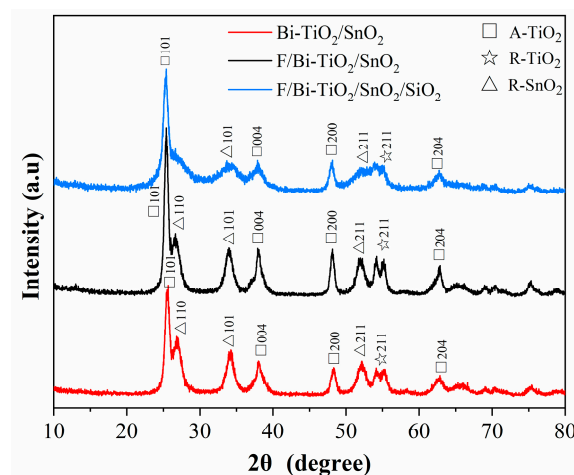

Figure 6. XRD patterns of Bi-TiO$_2$/SnO$_2$, F-Bi-TiO$_2$/SnO$_2$, and F-Bi-TiO$_2$/SnO$_2$/SiO$_2$.

Comparing the XRD spectra of F/Bi-TiO$_2$/SnO$_2$ and F/Bi-TiO$_2$/SnO$_2$/SiO$_2$, the introduction of SiO$_2$ reduced the intensity of the diffraction peaks of rutile SnO$_2$ and anatase TiO$_2$. This may be due to the hindrance of SnO$_2$ and TiO$_2$ grain growth when combined with SiO$_2$, resulting in smaller particle sizes (Table S1).

2.3.3. Nitrogen Adsorption Desorption Analysis

To obtain information about the pore structure and specific surface area of these catalysts, N$_2$ adsorption–desorption tests were conducted on Bi-TiO$_2$/SnO$_2$, F/Bi-TiO$_2$/SnO$_2$, and F/Bi-TiO$_2$/SnO$_2$/SiO$_2$ catalysts. The obtained adsorption–desorption isotherms are shown in Figure 7A. According to new classification by Donohue and Aranovich [59], the adsorption–desorption isotherms of the three catalysts are type (IV) isotherms with hysteresis loops. The BJH (Barrett–Joyner–Halenda) plot in Figure 7B indicated that the catalysts' pore size distribution was mainly between 2 and 25 nm, suggesting that these catalysts are mesoporous materials. Based on the Brunauer–Emmett–Teller equation, the specific surface

areas of Bi-TiO$_2$/SnO$_2$, F/Bi-TiO$_2$/SnO$_2$, and F/Bi-TiO$_2$/SnO$_2$/SiO$_2$ were calculated as 73.0, 69.1, and 112.27 m^2/g, respectively. It can be seen that F addition did not increase the specific surface area of the catalyst, while the addition of SiO$_2$ led to a significant increase in the specific surface area, which was likely due to SiO$_2$ forming a mesoporous material [57]. The increase in the specific surface area is beneficial for providing more adsorption and reactive sites for the reactants, thus enhancing the reaction efficiency.
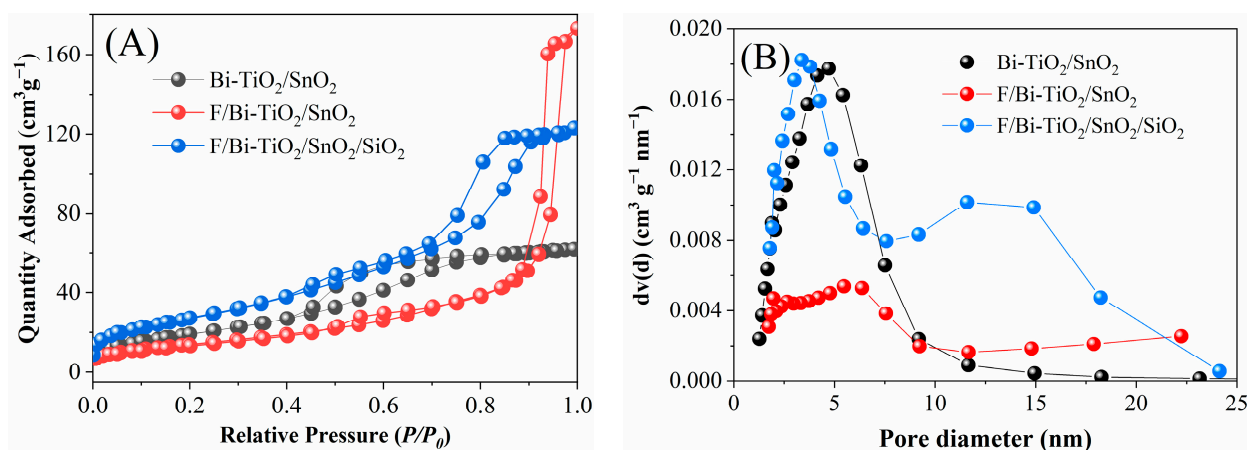

Figure 7. (**A**) N$_2$ adsorption–desorption isotherms and corresponding pore size distribution curves of Bi-TiO$_2$/SnO$_2$, F-Bi-TiO$_2$/SnO$_2$, and F-Bi-TiO$_2$/SnO$_2$/SiO$_2$. (**B**) The BJH plot.

2.3.4. Optical Properties

Figure 8A presents the UV-vis DRS for Bi-TiO$_2$/SnO$_2$, F/Bi-TiO$_2$/SnO$_2$, and F/Bi-TiO$_2$/SnO$_2$/SiO$_2$ catalysts. Compared with Bi-TiO$_2$/SnO$_2$, F/Bi-TiO$_2$/SnO$_2$ exhibited a significant red shift in the absorption edge, and the absorbance intensity in the UV and visible light regions was greatly enhanced. This indicated that fluoride ions, as dopants, alter the band structure of TiO$_2$, possibly due to an increase in the oxygen vacancy and Ti^{3+} defects introduced by fluorine doping into the TiO$_2$ lattice [47,60,61]. It reduced the bandgap and expanded the absorption range into the visible light region. Moreover, the absorption intensity was enhanced due to the formation of an intermediate level between the VB and CB of the metal oxide. The intermediate level can react as a trap to retard the charge recombination [28,62]. In comparison to F/Bi-TiO$_2$/SnO$_2$, further compositing with SiO$_2$ in F/Bi-TiO$_2$/SnO$_2$/SiO$_2$ did not cause a red shift in the absorption edge, and although there was an enhancement in UV absorption, there was no improvement in the visible light region. This is possibly due to no change in the structure of the metal oxides by composite with SiO$_2$. Instead, the role of SiO$_2$ was to inhibit the aggregation and growth of crystal grains and, more importantly, to provide a larger specific surface area, thereby increasing the adsorption and active site quantity for organic pollutants. Based on the Tauc plot (Figure 8B), the bandgaps of Bi-TiO$_2$/SnO$_2$, F/Bi-TiO$_2$/SnO$_2$, and F/Bi-TiO$_2$/SnO$_2$/SiO$_2$ were calculated as 2.97, 2.86, and 2.94 eV, respectively. It indicated that F doping reduced the bandgap of the photocatalyst and widened the visible light absorption range, while SiO$_2$ composite provided a larger specific surface area for the photocatalytic reaction, offering more reactive sites and dispersing the active sites.

To compare the separation efficiency of photo-generated carriers in the three catalysts, PL characterization was performed (Figure 8C). The PL spectra of the three catalysts show similar linear shapes. F and SiO$_2$ modifications, therefore, did not induce new fluorescence phenomena, indicating that fluorescence effects are primarily related to the microcrystalline surface structure of the catalyst. Compared to Bi-TiO$_2$/SnO$_2$ and F/Bi-TiO$_2$/SnO$_2$, the fluorescence intensity of F/Bi-TiO$_2$/SnO$_2$/SiO$_2$ significantly decreased, suggesting that both F modification and compositing with SiO$_2$ suppressed the recombination of photo-generated carriers. The reason probably lies in that F doping into TiO$_2$ and promotes the formation of lattice oxygen vacancies, which trap electrons and cause a decreased PL

intensity [47,63]. In addition, the role of SiO_2 is to disperse TiO_2 and SnO_2 grains on its surface, and then form a more favorable structure for the separation of photo-generated carriers, thereby elevating the photocatalytic efficiency.
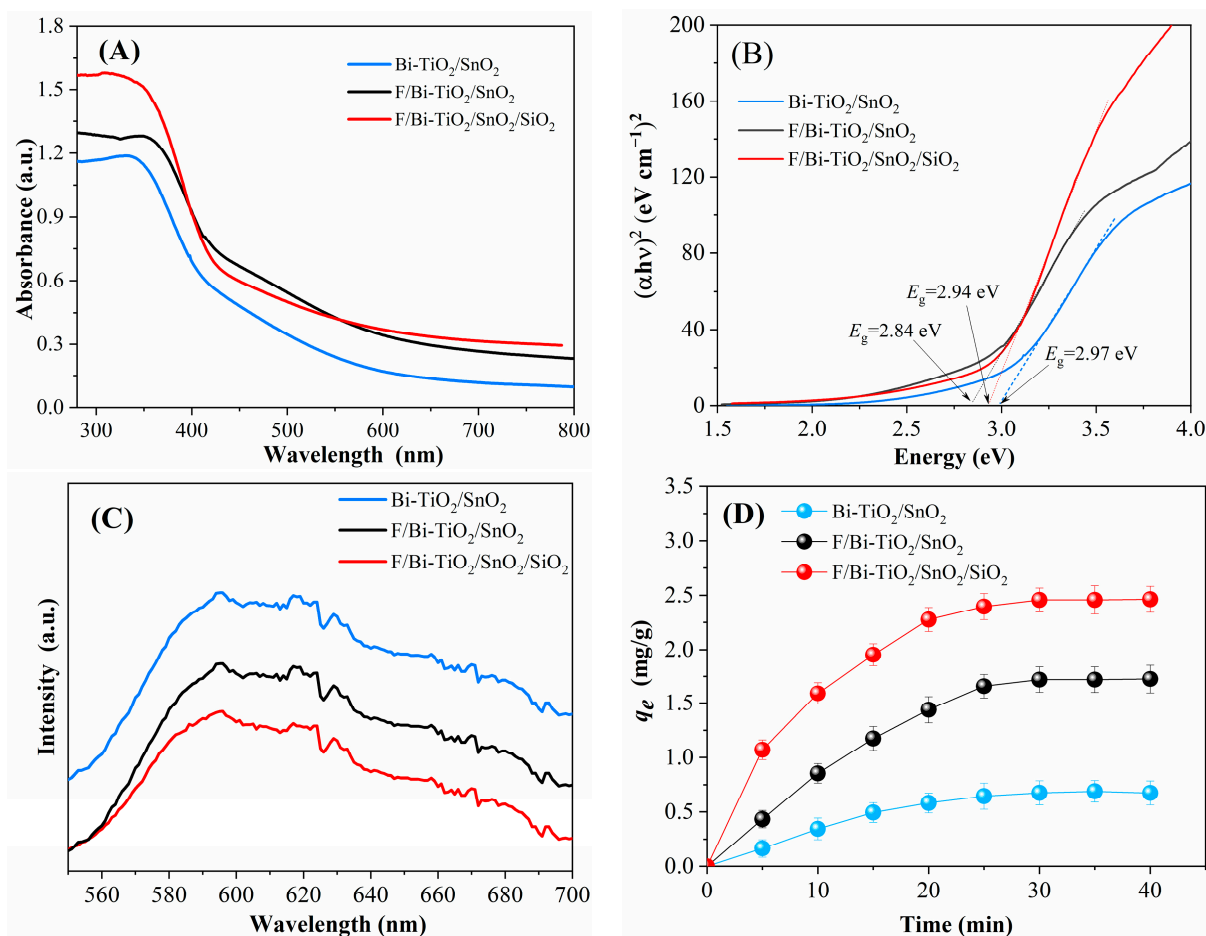

Figure 8. (**A**) UV–vis DRS of Bi-TiO_2/SnO_2, F/Bi-TiO_2/SnO_2, and F/Bi-$TiO_2/SnO_2/SiO_2$; (**B**) Tauc plot; (**C**) PL spectra; and (**D**) the amount of dark adsorption vs. adsorption time.

2.3.5. Adsorption Performance

To assess the influence of F doping and compositing with SiO_2 on the adsorption performance of the catalyst, the adsorption capacity of RhB in the dark was measured for Bi-TiO_2/SnO_2, F/Bi-TiO_2/SnO_2, and F/Bi-$TiO_2/SnO_2/SiO_2$, as shown in Figure 8D. The saturated adsorption capacities of the three catalysts for RhB were 0.67, 1.72, and 2.46 mg/g, respectively. It was evident that both F modification and SiO_2 modification increase the adsorption capacity of the catalyst for RhB molecules. The reason for the increased adsorption capacity with F modification may be that, although F did not increase the specific surface area of the catalyst, it increased the surface acidic sites that tend to adsorb basic Rhodamine B molecules. Moreover, the surface acidic sites are in favor of converting adsorbed H_2O to OH, and subsequently, more surface hydroxyl radicals with strong mobility are generated [64]. While SiO_2 modification did not increase the catalyst's absorption of visible light, it contributed to the increase in the specific surface area. This resulted in the dispersion of more active sites on the catalyst surface for adsorbing reactants, thereby increasing the adsorption capacity of reactants and promoting the progression of the reaction.

2.4. Impact of F and SiO$_2$ Addition on RhB Photocatalytic Degradation

2.4.1. Impact of F Doping on RhB Degradation

The optimal doping amount of F was determined by testing the photocatalytic activity of F/Bi-TiO$_2$/SnO$_2$ with different F doping amounts (Figure 9A). As observed, with the increase in F addition amounts, the photocatalytic activity of F/Bi-TiO$_2$/SnO$_2$ initially increased and then decreased. The catalyst exhibited the highest activity when the molar ratio of F to Ti was 0.2, achieving an RhB degradation ratio of 96% after 60 min of reaction. The RhB degradation processes were fitted by the pseudo-first-order model (Figure 9B). The results showed that the reaction rate constants (*k*) for Bi-TiO$_2$/SnO$_2$ and F/Bi-TiO$_2$/SnO$_2$ (F/Ti = 0.2) were determined to be 0.042 and 0.098 min^{-1} (Figure S2), respectively, indicating that F doping increased the reaction rate constant by 2.3 times compared to the Bi-TiO$_2$/SnO$_2$. A small amount of doping (F/Ti = 0.1, 0.2) was more favorable for enhancing catalyst activity. One possible reason is that a small amount of fluoride ions enters the TiO$_2$ lattice and occupies the O positions, causing lattice defects such as oxygen vacancy. These defects provide locations for electrons and facilitate the transfer of photo-generated carriers. Additionally, the doping ions may introduce impurity states within the bandgap, which hybridize with the energy bands of TiO$_2$. This ensures the efficient transfer of photo-generated carriers to the surface active sites, thereby increasing the absorption of sunlight. However, an excess of F ions decreased the catalyst's activity, potentially due to the generation of a negative electric potential that inhibited electron migration to the catalyst surface and increased the electron–hole pair recombination. Excessive doping concentrations may also lead to more severe lattice expansion, increased particle size, and a decrease in photocatalytic efficiency.
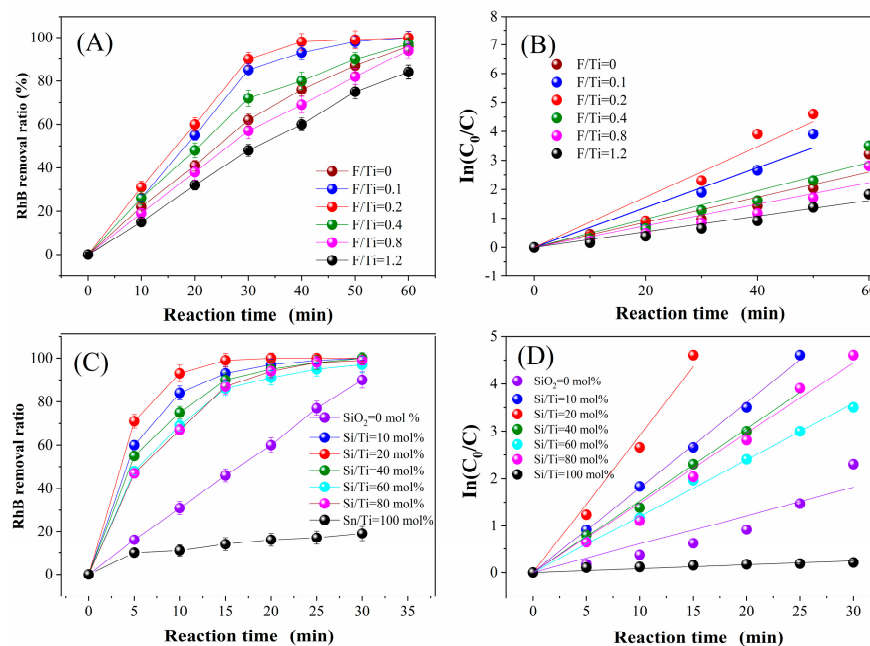

Figure 9. (**A**) Photocatalytic removal curves and (**B**) pseudo-first-order kinetics curves for the degradation of RhB by F/Bi-TiO$_2$/SnO$_2$ with different F amounts, and (**C**) photocatalytic removal curves and (**D**) pseudo-first-order kinetics curves of F/Bi-TiO$_2$/SnO$_2$/SiO$_2$ with different SiO$_2$/SnO$_2$ molar ratios.

2.4.2. Impact of SiO$_2$/SnO$_2$ Molar Ratio on RhB Degradation

The impact of the SiO$_2$/SnO$_2$ molar ratio on the photocatalytic activity was investigated. Figure 9C depicts the degradation efficiency of RhB over time for F/Bi-TiO$_2$/SnO$_2$/SiO$_2$ catalysts with different SiO$_2$/SnO$_2$ molar ratios. It can be seen that, with an increase in the SiO$_2$ addition level, the catalytic activity initially increased and then decreased. The catalyst exhibited the highest degradation ratio of RhB when the SiO$_2$/SnO$_2$

molar ratio was 20 mol%, reaching over 90% in 10 min with a reaction rate constant of 0.291 min^{-1} based on pseudo-first-order fitting (Figures 9D and S2). This indicated that an appropriate amount of SiO$_2$ composite was conducive to enhancing photocatalytic activity. Considering the characterization results, this improvement was likely due to the SiO$_2$/SnO$_2$ composite having a certain porosity, which improved the porous structure and increased the specific surface area, thereby facilitating the adsorption and degradation of RhB on the catalyst surface. However, excessive SiO$_2$ may cover the active sites of the catalyst, reducing light absorption and the contact points between active components and the reactants, limiting photocatalytic performance.

By the optimization of the addition amounts of Bi, SnO$_2$, F, and SiO$_2$, the RhB degradation percentage was close to 100% after 20 min of irradiation under simulated sunlight. Table 1 lists the catalytic degradation effects of some similar catalysts on Rhodamine B degradation in some studies.

Table 1. Statistics of photocatalytic degradation of RhB with different photocatalysts.

Composite	Light	Concentration	D (%)	Time (min)
SnO$_2$/TiO$_2$/PVDF [65]	UV	10 mg/L	91.84	270
SnO$_2$/TiO$_2$/RGO [66]	UV	10 mg/L	97.60	40
SnO$_2$–TiO$_2$ [67]	Visible	10^{-5} mol/L	76.00	180
S doped SnO$_2$ @TiO$_2$ [68]	Sunlight	10 mg/L	97.00	200
SnO$_2$/TiO$_2$ [69]	UV–vis	10 mg/L	99.00	30
SnO$_2$/TiO$_2$ [70]	UV–vis	20 mg/L	94.00	180
SnO$_2$/TiO$_2$ [39]	UV–vis	10 mg/L	98.00	120
B-TiO$_2$/SnO$_2$ [54]	VisibleUV–vis	10 mg/L	96.62100	9070
O-g-C$_3$N$_4$/SnO$_2$ [71]	Visible	10 mg/L	98.10	30
Bi/Bi$_2$O$_3$/TNAs [24]	Sunlight	2 mg/L	35	240
Bi/BPNs/P–BiOCl [72]	Xenon lamp	20 mg/L	100	30
KF/Bi/BC [55]	Xenon lamp	30 mg/L	100	10
C/F–Ag–TiO$_2$ [73]	Xenon lamp	10 mg/L	84.2	240
N,F-TiO$_{2-\delta}$ [74]	LED lights	10 mg/L	77.2	60
F/Bi-TiO$_2$/SnO$_2$/SiO$_2$ (this study)	Xenon lamp	10 mg/L	100	20

2.4.3. Cyclic Use of the Photocatalyst

The stability of the optimal F/Bi-TiO$_2$/SnO$_2$/SiO$_2$ was assessed through cyclic RhB degradation tests, with each reaction lasting 30 min. After each reaction, the catalyst was rinsed several times with deionized water, dried, and then reused for subsequent reactions. The results shown in Figure 10A indicated that there was little attenuation in catalytic performance after five repeated reactions. However, the degradation ratio of RhB could still reach 100% within 30 min, indicating the stability of the F/Bi-TiO$_2$/SnO$_2$/SiO$_2$ catalyst.

2.4.4. Effect of pH Value on Catalytic Activity

In this experiment, the natural pH of the reaction solution was around 7. The pH of the reaction system was adjusted using 0.01 mol/L NaOH and 0.01 mol/L HNO$_3$ solutions. The activity test results shown in Figure 10B revealed that the pH value significantly influenced the activity of F/Bi-TiO$_2$/SnO$_2$/SiO$_2$ in RhB degradation. The degradation performance of RhB within 30 min followed the order: neutral (pH = 7) > slightly acidic (pH = 5) > slightly alkaline (pH = 9) > highly alkaline (pH = 11) > highly acidic (pH = 3). The reaction rate initially increased and then decreased with an increase in the pH value. The fastest reaction rate was observed at pH = 7, indicating the best performance under neutral conditions, and both highly acidic and highly alkaline environments were unfavorable for the photocatalytic reaction. The reason lies in the impact of pH changes on the charge distribution on the catalyst surface and on the reactant molecular structure [52], which affect the adsorption capacity of the catalyst for RhB molecules. In highly alkaline conditions, hydrogen ions in the surface hydroxyl groups are replaced by cations, resulting in a decrease in the number of surface hydroxyl groups. The hydroxyl groups are in favor of

oxidation of organic pollutants. When it comes to highly acidic conditions, the positive charge is carried by the catalyst. Since RhB is a cationic dye [75], the increased positive charge diminishes the adsorption capacity of the catalyst for RhB, thereby hindering the photocatalytic degradation of RhB. Typically, the pH of dye wastewater ranges from 6 to 10. The optimal pH for the $F/Bi-TiO_2/SnO_2/SiO_2$ photocatalytic reaction in RhB degradation was found to be 7, with a degradation efficiency reaching 93.89% within 10 min. Moreover, pH 7 is more adaptable to the pH variations typically found in dyeing wastewater.
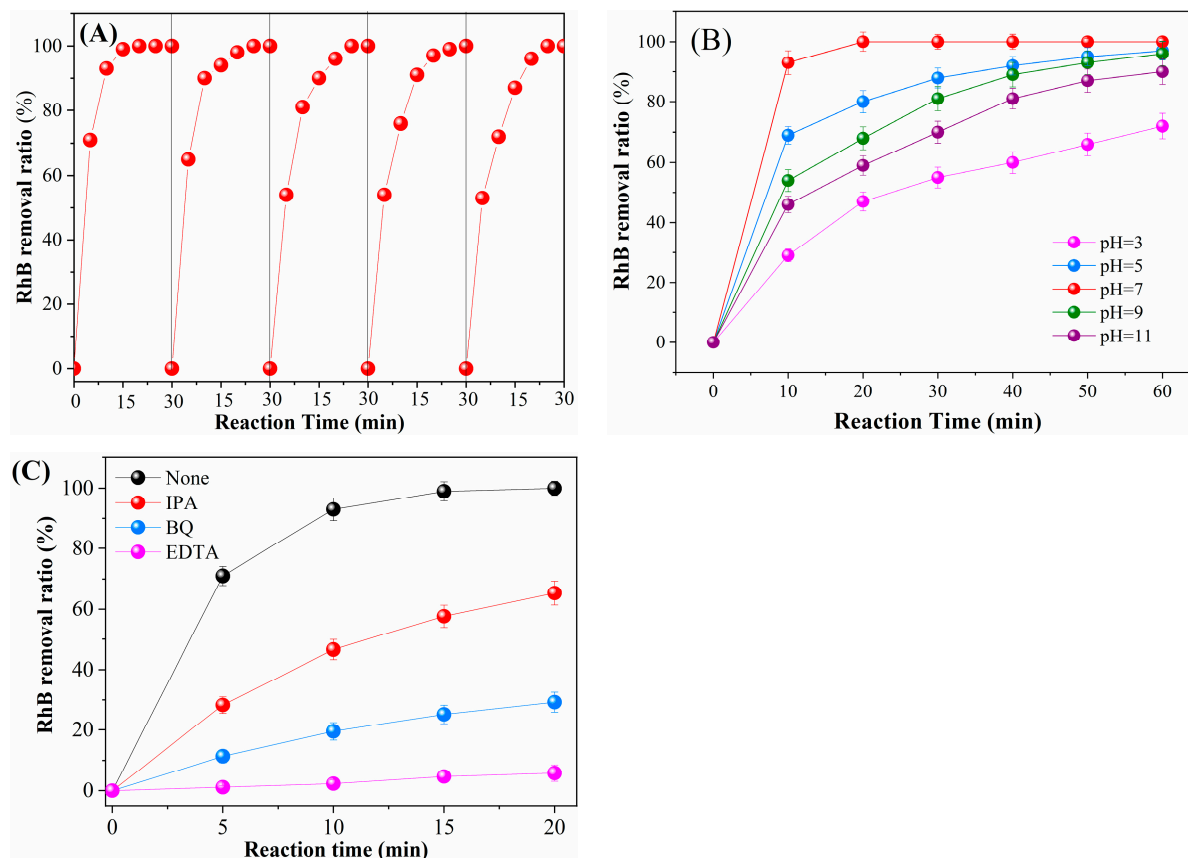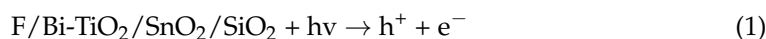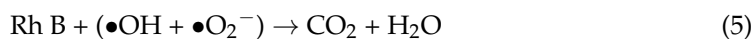

Figure 10. (**A**) Cyclic RhB degradation tests with $F/Bi-TiO_2/SnO_2/SiO_2$. (**B**) Effect of pH on the degradation of RhB with $F/Bi-TiO_2/SnO_2/SiO_2$. (**C**) Effects of sacrificial agents on photo-degradation of RhB with $F/Bi-TiO_2/SnO_2/SiO_2$.

2.4.5. Investigation of Active Species

The optimal amount of $F/Bi-TiO_2/SnO_2/SiO_2$ was used, and several sacrificial agents were added to the RhB solution to distinguish the main active species during the RhB degradation process. IPA, EDTA, and BQ were selected to be radical quenchers for OH, h^+, and O_2^-, respectively. Figure 10C shows that the RhB degradation ratio after 20 min of reaction decreased from 100% to 65%, 29%, and 6% when IPA, BQ, and EDTA were added, respectively. The results revealed that all of the corresponding $\bullet OH$, $\bullet O_2^-$, and h^+ participate in the photo-degradation reaction and play an important role. The most crucial active species was h^+ according to the lowest RhB degradation ratio with EDTA addition. It implies that the oxidation of water to introduce OH radicals by a photo-generated h^+ assumes a key role in the process of RhB oxidation. The reaction mechanism was speculated as follows:

$$F/Bi-TiO_2/SnO_2/SiO_2 + h\nu \rightarrow h^+ + e^- \tag{1}$$

$$h^+ + H_2O \rightarrow H^+ + \bullet OH \tag{2}$$

$$h^+ + OH^- \rightarrow \bullet OH \tag{3}$$

$$O_2 + e^- \rightarrow \bullet O_2^- \qquad (4)$$

$$Rh\,B + (\bullet OH + \bullet O_2^-) \rightarrow CO_2 + H_2O \qquad (5)$$

3. Discussion

Based on the characterization test, the impact of the Bi and F doping and compositing with SnO_2 and SiO_2 on the catalyst's performance was analyzed. The results indicated that Bi addition induced a loose and porous surface of the catalyst. Doping Bi into the TiO_2 lattice formed electron interactions with TiO_2 in the form of $Bi^{3+\sigma}$, potentially generating more oxygen vacancies that act as traps for photo-generated electrons and impede the recombination of electron–hole pairs. Additionally, Bi doping improved UV light-harvesting properties, while the combination with SnO_2 can improve the absorption of visible and ultraviolet light. The SnO_2 and F modification suppressed the recombination of photo-induced carriers. The doping of fluorine may elevate the oxygen vacancy and hybrid level, which reduced the bandgap and increased visible light absorption. In addition, the adsorption ability toward RhB molecules on catalyst's surface was advanced by F addition, which may be due to the increase in acidity. The composited SiO_2 contributed by providing a larger specific surface area for the adsorption of more RhB molecules. Benefiting from the effect of doped F and Bi atoms in the combination with SnO_2 and SiO_2, the recombination of photo-excited electrons and holes is inhibited, and the adsorption of the reactant molecules is increased, thus improving the activity of the catalyst.

4. Materials and Methods

4.1. Material and Reagents

Tetrachlorostannane pentahydrate ($SnCl_4 \cdot 5H_2O$, Sigma-Aldrich, St. Louis, MO, USA, AR/99.99%), Bismuth nitrate pentahydrate ($Bi(NO_3) \cdot 5H_2O$, Sigma-Aldrich, St. Louis, MO, USA, AR/99.0%), Polyethylene glycol (PEG-1000, Tianjin Kemiou Chemical Reagent Co., Ltd., Tianjin, China, AR), Urea ($CO(NH_2)_2$, Sinopharm, Beijing, China, AR/99.5%), Tetraethl silicate (TEOS, Tianjin Kemiou Chemical Reagent Co., Ltd., Tianjin, China, AR/99.0%), Ethyl alcohol (EtOH, Sinopharm, Beijing, China, AR/99.5%), Hydrofluoric acid (HF, Tianjin Kemiou Chemical Reagent Co., Ltd., Tianjin, China, AR/50%), Titanium butoxide (TBT, aladdin, Bay City, MI, USA, AR/99%), Hydrochloric acid (HCl, Sinopharm, Beijing, China, AR/36%~38%), Iso-propyl alcohol (IPA, Sigma-Aldrich, St. Louis, MO, USA, AR/99.5%), benzoquinone (BQ, Sigma-Aldrich, St. Louis, MO, USA, AR/99.5%), and EDTA (Sigma-Aldrich, St. Louis, MO, USA, AR/99.5%).

All data processing was conducted using Origin Pro 2018 (OriginLab, Northampton, MA, USA). XRD data analysis was performed using Jade version 5.0 (Materials Data Inc., Livermore, CA, USA).

4.2. Preparation of Photocatalysts

4.2.1. Synthesis of Bi-TiO$_2$/SnO$_2$

Firstly, SnO_2 was prepared using a precipitation method described in the Supplementary Materials. Then, Bi-TiO_2/SnO_2 was prepared using a sol–gel method: A certain volume of EtOH and TBT, in a volume ratio of 5:13, was measured. TBT was then slowly added drop by drop into EtOH. Then, the mixture was covered with plastic wrap and magnetically stirred for 20 min to obtain Solution A. After that, EtOH, deionized water, and CH_3COOH were measured in a volume ratio of 21:1:4 and mixed uniformly. $Bi(NO_3)_3 \cdot 5H_2O$ was added to the mixture (Bi/Ti = 0.7 mol%), and the solution was sonicated for 30 min to form Solution B. Solution B was transferred into a pear-shaped funnel and slowly added drop by drop into continuously stirred Solution A. The mixture was then covered with plastic wrap and stirred for 2 h until a wall-sticking phenomenon was observed when gently tilting the beaker. The plastic wrap was removed, and a certain amount of the previously prepared SnO_2 was added based on a Sn/Ti molar ratio of 1:4. The mixture was then stirred until the stir bar could no longer rotate; at which point, a sol was formed. The sol–gel was aged at room temperature for 24 h and then dried in an 80 °C oven for 24 h until a dry gel was

obtained. The gel was ground and calcined in a muffle furnace at 400 °C for 2 h to yield the Bi-TiO$_2$/SnO$_2$ powder.

4.2.2. Synthesis of F-Bi-TiO$_2$/SnO$_2$

The steps were identical to those in Section 4.2.1, with the only difference being the addition of hydrofluoric acid (50%) to Solution B in a certain F/Ti molar ratio as the precursor for fluorine.

4.2.3. Synthesis of F-Bi-TiO$_2$/SnO$_2$/SiO$_2$

First, a SnO$_2$/SiO$_2$ composite gel was prepared: A mixture solution of TEOS, anhydrous ethanol, and HCl (molar ratio of 1:6:0.02) was prepared. The solution was stirred thoroughly to obtain a transparent SiO$_2$ sol, which was left at room temperature for 60 min. A 1.5×10^{-3} mol/L SnCl$_4$ aqueous solution was prepared, and SnCl$_4$ was slowly added to the SiO$_2$ sol in a certain molar ratio. Ammonia solution was dropwise added to the mixture under continuous stirring until the pH reached 7.0. After aging for 2 days at room temperature, the gel was filtered and washed with water until free of Cl$^-$ ions (tested with 0.1 mol/L AgNO$_3$ solution). Finally, the gel was dried in an oven at 60 °C to obtain the SnO$_2$/TiO$_2$ composite gel.

Subsequently, the sol–gel method, as described in Section 4.2.2, was used. The difference was that the SnO$_2$ added was replaced with the SnO$_2$/SiO$_2$ composite gel. The final product was F-Bi-TiO$_2$/SnO$_2$/SiO$_2$.

4.3. Catalyst Evaluation

An experimental device (Figure S1) was employed for photocatalytic activity evaluation. A self-made quartz glass reactor, with a height of 100 mm and an inner diameter of 62 mm, was used, featuring a sampling port on the side. Continuous stirring of the solution in the reactor was achieved using a magnetic stirrer to ensure sufficient contact between the catalyst and the solution. The light source, i.e., a 350 W spherical xenon lamp, was positioned 15 cm vertically above the reactor to simulate solar light. During illumination, a blower was used for cooling the air in the xenon lamp, and circulating cooling water was utilized to ensure that the reaction occurred at room temperature. Rhodamine B (RhB) was chosen as the target for degradation to investigate the activity of the catalyst, with an initial concentration of 10 mg/L. The prepared catalyst was added to the solution under stirring, with a catalyst dosage of 1 g/L. The reactor was sealed with quartz plates and in darkness. The solution was stirred for 30 min to reach the adsorption–desorption equilibrium. The adsorption equilibrium time was determined through dark adsorption experiments. The xenon lamp was then turned on to initiate irradiation. During the reaction, at regular intervals, 4 mL of solution was withdrawn using a syringe. The concentration of Rhodamine B in the samples was detected using a UV-2450 (Shimadzu, Beijing, China) UV-vis spectrophotometer, and the removal efficiency of RhB was calculated using Equation as follows: $D = (C_0 - C_t)/C_0$. Wherein D is the degradation efficiency of RhB (%); C_0 and C_t represent the RhB concentration at 0 and t min, respectively. In addition, the RhB degradation processes were fitted by a pseudo-first-order model using the following equation: $\ln(C_0/C_t) = kt$, where k is the reaction rate constant.

4.4. Catalyst Characterizations

X-ray diffraction (XRD) pattern of the catalysts was recorded using a D/Max 2500PC diffractometer (Rigaku, Akishima, Japan) with Cu Ka radiation. Scans were collected in the 2θ range of 10~80° and a step of 4 °/min. The crystallite size was calculated based on the Scherrer equation. X-ray photoelectron spectroscopy (XPS) measurement was performed with a *K-Alpha*$^+$ (Thermo fisher Scientific, Waltham, MA, USA). Al Kα was used as a radiation source. The binding energy of C1s was used for correction. The micromorphologies of the samples were obtained with a S4800 scanning electron microscopy (SEM) (Rigaku, Japan). The specific surface area, pore size, and pore volume of the catalysts were measured

by an automatic constant-volume adsorption instrument (Belsorp II, Bayer Japan Co., Ltd., Chiyoda, Japan). Before nitrogen adsorption, the catalyst was pretreated in vacuum at 400 °C for 3 h. The nitrogen adsorption–desorption process was carried out at the liquid nitrogen temperature (77 K). The light absorption capacity of the catalysts was recorded by barium sulfate tablet method with a UV-2540 UV-vis spectrophotometer (Shimadzu, Tokyo, Japan) in the wavelength range of 200~800 nm. The bandgaps were computed via the Tauc and Menth Equation.

$$\alpha h v = A(h v - E_g)^n \tag{6}$$

where α is the absorptivity, h is the Planck's constant, v is the frequency of radiation, E_g is the bandgap, A is the constant of proportionality, and n is the type of optical transition following photon absorption.

Fluorescence analysis was obtained using a FluoroMax-4 photoluminescence spectrometer (HORIBA Scientific, Irvine, CA, USA) with a wavelength scanning range of 350~700 nm, step size of 0.1 s, and slit size of 2 nm.

5. Conclusions

The TiO_2 was modified by co-doping with Bi and F and compositing with SnO_2 and SiO_2. The synthesized catalyst demonstrated efficient photocatalytic performance toward RhB degradation under simulated sunlight. Through the optimization of the doping levels of Bi and F, as well as the ratio of SnO_2 and SiO_2 composite, the catalyst reached a degradation efficiency of 100% for RhB within 20 min under simulated sunlight, with a first-order reaction rate constant of 0.291 min^{-1}. This optimal catalyst showed stability in the cycle tests. The reaction rate initially increased and then decreased with an increase in the pH value. The active species h^+ assume a key role in the process of RhB oxidation. The combined effects of Bi, F, Sn, and Si modifications include the following: (1) enhanced absorbance intensity in the UV and visible light regions; (2) reduced recombination of photo-generated carriers; and (3) increased specific surface area that provides more adsorption sites for reactant molecules. Because of these beneficial modifications, the catalyst exhibited excellent photocatalytic activity for RhB degradation under simulated sunlight.

References

1. Raizada, P.; Sudhaik, A.; Singh, P.; Shandilya, P.; Gupta, V.K.; Hosseini-Bandegharaei, A.; Agrawal, S. Ag_3PO_4 modified phosphorus and sulphur co-doped graphitic carbon nitride as a direct Z-scheme photocatalyst for 2, 4-dimethyl phenol degradation. *J. Photochem. Photobiol. A* **2019**, *374*, 22–35. [CrossRef]
2. Mendoza-Diaz, M.-I.; Lecestre, A.; Salvagnac, L.; Bounor, B.; Pech, D.; Djafari-Rouhani, M.; Esteve, A.; Rossi, C. High surface area TiO_2 photocatalyst for H_2 production through silicon micromachining. *Appl. Surf. Sci.* **2022**, *588*, 152919. [CrossRef]

3. Kim, H.; Lee, J.; Yantara, N.; Boix, P.P.; Kulkarni, S.A.; Mhaisalkar, S.; Grätzel, M.; Park, N.G. High Efficiency Solid-State Sensitized Solar Cell-Based on Submicrometer Rutile TiO_2 Nanorod and $CH_3NH_3PbI_3$ Perovskite Sensitizer. *Nano Lett.* **2013**, *13*, 2412–2417. [CrossRef] [PubMed]

4. Cui, X.; Li, H.; Yang, Z.; Li, Y.; Zhang, P.; Zheng, Z.; Wang, Y.; Li, J.; Zhang, X. A novel $CaIn_2S_4/TiO_2NTAs$ heterojunction photoanode for highly efficient photocathodic protection performance of 316 SS under visible light. *Nanotechnology* **2021**, *32*, 395702. [CrossRef] [PubMed]

5. Zhang, G.; Zhang, Y.C.; Nadagouda, M.; Han, C.; O′Shea, K.; El-Sheikh, S.M.; Ismail, A.A.; Dionysiou, D.D. Visible light-sensitized S, N and C co-doped polymorphic TiO_2 for photocatalytic destruction of microcystin-LR. *Appl. Catal. B Environ.* **2014**, *144*, 614–621. [CrossRef]

6. Isari, A.A.; Hayati, F.; Kakavandi, B.; Rostami, M.; Motevassel, M.; Dehghanifard, E. N, Cu co-doped TiO_2@functionalized SWCNT photocatalyst coupled with ultrasound and visible-light: An effective sono-photocatalysis process for pharmaceutical wastewaters treatment. *Chem. Eng. J.* **2020**, *392*, 123685. [CrossRef]

7. Ismael, M. Enhanced photocatalytic hydrogen production and degradation of organic pollutants from Fe (III) doped TiO_2 nanoparticles. *J. Environ. Chem. Eng.* **2020**, *8*, 103676. [CrossRef]

8. Meng, A.; Zhang, L.; Cheng, B.; Yu, J. Dual Cocatalysts in TiO_2 Photocatalysis. *Adv. Mater.* **2019**, *31*, 1807660. [CrossRef]

9. Moon, H.S.; Hsiao, K.; Wu, M.; Yun, Y.; Hsu, Y.; Yong, K. Spatial separation of cocatalysts on Z-Scheme organic/inorganic heterostructure hollow spheres for enhanced photocatalytic H_2 evolution and in-depth analysis of the charge-transfer mechanism. *Adv. Mater.* **2022**, *35*, 2200172. [CrossRef]

10. Kumar, A.; Khan, M.; He, J.; Lo, I.M. Recent developments and challenges in practical application of visible-light-driven TiO_2-based heterojunctions for PPCP degradation: A critical review. *Water Res.* **2020**, *170*, 115356. [CrossRef]

11. Meng, A.; Cheng, B.; Tan, H.; Fan, J.; Su, C.; Yu, J. TiO_2/polydopamine S-scheme heterojunction photocatalyst with enhanced CO_2-reduction selectivity. *Appl. Catal. B Environ.* **2021**, *289*, 120039. [CrossRef]

12. Liang, Z.; Bai, X.; Hao, P.; Guo, Y.; Xue, Y.; Tian, J.; Cui, H. Full solar spectrum photocatalytic oxygen evolution by carbon-coated TiO_2 hierarchical nanotubes. *Appl. Catal. B Environ.* **2019**, *243*, 711–720. [CrossRef]

13. Singh, J.; Juneja, S.; Soni, R.K.; Bhattacharya, J. Sunlight mediated enhanced photocatalytic activity of TiO_2 nanoparticles functionalized CuO-Cu_2O nanorods for removal of methylene blue and oxytetracycline hydrochloride. *J. Colloid Interf. Sci.* **2021**, *590*, 60–71. [CrossRef] [PubMed]

14. Yu, C.; Zhou, W.; Yang, K.; Rong, G. Hydrothermal synthesis of hemisphere-like F-doped anatase TiO_2 with visible light photocatalytic activity. *J. Mater. Sci.* **2010**, *45*, 5756–5761. [CrossRef]

15. Wang, Y.; Zhang, Y.; Zhu, X.; Liu, Y.; Wu, Z. Fluorine-induced oxygen vacancies on TiO_2 nanosheets for photocatalytic indoor VOCs degradation. *Appl. Catal. B Environ.* **2022**, *316*, 121610. [CrossRef]

16. Tosoni, S.; Lamiel-Garcia, O.; Fernandez, H.; Doña, J.M.; Illas, F. Electronic Structure of F-Doped Bulk Rutile, Anatase, and Brookite Polymorphs of TiO_2. *J. Phys. Chem. C* **2012**, *116*, 12738–12746. [CrossRef]

17. Pang, D.; Wang, Y.; Ma, X.; Ouyang, F. Fluorine promoted and silica supported TiO_2 for photocatalytic decomposition of acrylonitrile under simulant solar light irradiation. *Chem. Eng. J.* **2014**, *258*, 43–50. [CrossRef]

18. Wen, J.; Li, X.; Liu, W.; Fang, Y.; Xie, J.; Xu, Y. Photocatalysis fundamentals and surface modification of TiO_2 nanomaterials. *Chin. J. Catal.* **2015**, *36*, 2049–2070. [CrossRef]

19. Chakinala, N.; Gogate, P.R.; Chakinala, A.G. Highly efficient bi-metallic bismuth-silver doped TiO_2 photocatalyst for dye degradation. *Korean J. Chem. Eng.* **2021**, *38*, 2468–2478. [CrossRef]

20. Liang, Z.; Cao, Y.; Li, Y.; Xie, J.; Guo, N.; Jia, D. Solid-state chemical synthesis of rod-like fluorine-doped β-Bi_2O_3 and their enhanced photocatalytic property under visible light. *Appl. Surf. Sci.* **2016**, *390*, 78–85. [CrossRef]

21. Cao, W.; Wang, W.; Yang, Z.; Wang, W.; Chen, W.; Wu, K. Enhancing photocathodic protection performance by controlled synthesis of $Bi/BiOBr/TiO_2$ NTAs Z-scheme heterojunction films. *J. Alloys Compd.* **2023**, *960*, 170675. [CrossRef]

22. Reddy, P.A.K.; Srinivas, B.; Kala, P.; Kumari, V.D.; Subrahmanyam, M. Preparation and characterization of Bi-doped TiO_2 and its solar photocatalytic activity for the degradation of isoproturon herbicide. *Mater. Res. Bull.* **2011**, *46*, 1766–1771. [CrossRef]

23. Huang, J.; Cheuk, W.; Wu, Y.; Lee, F.S.; Ho, W. Fabrication of Bi-Doped TiO_2 spheres with ultrasonic spray pyrolysis and investigation of their visible-light photocatalytic properties. *J. Nanotechnol.* **2012**, *2012*, 214783. [CrossRef]

24. Althamthami, M.; Guettaf Temam, E.; Temam, H.B.; Saâd, R. Improved photocatalytic activity under the sunlight of high transparent hydrophilic Bi-doped TiO_2 thin-films. *J. Photochem. Photobiol. A* **2023**, *443*, 114818. [CrossRef]

25. Murcia-López, S.; Hidalgo, M.C.; Navío, J.A. Synthesis, characterization and photocatalytic activity of Bi-doped TiO_2 photocatalysts under simulated solar irradiation. *Appl. Catal. A Gen.* **2011**, *404*, 59–67. [CrossRef]

26. Li, D.; Zhang, Y.; Zhang, Y.; Zhou, X.; Guo, S. Fabrication of bidirectionally doped β-Bi_2O_3/TiO_2-NTs with enhanced photocatalysis under visible light irradiation. *J. Hazard. Mater.* **2013**, *258–259*, 42–49. [CrossRef]

27. Liu, Z.; Wang, Q.; Tan, X.; Zheng, S.; Zhang, H.; Wang, Y.; Gao, S. Solvothermal preparation of Bi/Bi_2O_3 nanoparticles on TiO_2 NTs for the enhanced photoelectrocatalytic degradation of pollutants. *J. Alloys Compd.* **2020**, *815*, 152478. [CrossRef]

28. Mohamed, I.M.A.; Dao, V.; Yasin, A.S.; Mousa, H.M. Nitrogen-doped&SnO_2-incoportaed TiO_2 nanofibers as novel and effective photoanode for enhanced efficiency dye-sensitized solar cells. *Chem. Eng. J.* **2016**, *304*, 48–60.

29. Chawla, A.; Sudhaik, A.; Raizada, P.; Khan, A.A.P.; Singh, A.; Van Le, Q.; Nguyen, V.H.; Ahamad, T.; Alshehri, S.M.; Asiri, A.M.; et al. An overview of SnO$_2$ based Z scheme heterojuctions: Fabrication, mechanism and advanced photocatalytic applications. *J. Ind. Eng. Chem.* **2022**, *116*, 515–542. [CrossRef]

30. Roy, H.; Rahman, T.U.; Khan, M.A.J.R.; Al-Mamun, M.R.; Islam, S.Z.; Khaleque, M.A.; Hossain, M.I.; Khan, M.Z.H.; Islam, M.S.; Marwani, H.M.; et al. Toxic dye removal, remediation, and mechanism with doped SnO$_2$-based nanocomposite photocatalysts: A critical review. *J. Water Process Eng.* **2023**, *54*, 104069. [CrossRef]

31. Pesci, F.M.; Wang, G.; Klug, D.R.; Li, Y.; Cowan, A.J. Efficient suppression of electron-hole recombination in oxygen-deficient hydrogen-treated TiO$_2$ nanowires for photoelectrochemical water splitting. *J. Phys. Chem. C Nanomater. Interfaces* **2013**, *117*, 25837–25844. [CrossRef] [PubMed]

32. Kusior, A.; Zych, L.; Zakrzewska, K.; Radecka, M. Photocatalytic activity of TiO$_2$/SnO$_2$ nanostructures with controlled dimensionality/complexity. *Appl. Surf. Sci.* **2019**, *471*, 973–985. [CrossRef]

33. Alagarasi, A.; Rajalakshmi, P.U.; Shanthi, K.; Selvam, P. Solar-light driven photocatalytic activity of mesoporous nanocrystalline TiO$_2$, SnO$_2$, and TiO$_2$-SnO$_2$ composites. *Mater. Today Sustain.* **2019**, *5*, 100016. [CrossRef]

34. Magdalane, C.M.; Kanimozhi, K.; Arularasu, M.V.; Ramalingam, G.; Kaviyarasu, K. Self-cleaning mechanism of synthesized SnO$_2$/TiO$_2$ nanostructure for photocatalytic activity application for waste water treatment. *Surf. Interfaces* **2019**, *17*, 100346. [CrossRef]

35. De Mendonça, V.R.; Avansi, W.; Arenal, R.; Ribeiro, C. A building blocks strategy for preparing photocatalytically active anatase TiO$_2$/rutile SnO$_2$ heterostructures by hydrothermal annealing. *J. Colloid Interface Sci.* **2017**, *505*, 454–459. [CrossRef]

36. Angel, R.D.; Durán-Álvarez, J.; Zanella, R. TiO$_2$-low band gap semiconductor heterostructures for water treatment using sunlight-Driven photocatalysis. *Titan. Dioxide Mater. Sustain. Environ.* **2018**, *76501*, 305–329.

37. Albornoz, L.L.; Da Silva, S.W.; Bortolozzi, J.P.; Banús, E.D.; Brussino, P.; Ulla, M.A.; Bernardes, A.M. Degradation and mineralization of erythromycin by heterogeneous photocatalysis using SnO$_2$-doped TiO$_2$ structured catalysts: Activity and stability. *Chemosphere* **2021**, *268*, 128858. [CrossRef]

38. Rajput, R.B.; Jamble, S.N.; Kale, R.B. A review on TiO$_2$/SnO$_2$ heterostructures as a photocatalyst for the degradation of dyes and organic pollutants. *J. Environ. Manag.* **2022**, *307*, 114533. [CrossRef]

39. Hassan, S.M.; Ahmed, A.I.; Mannaa, M.A. Structural, photocatalytic, biological and catalytic properties of SnO$_2$/TiO$_2$ nanoparticles. *Ceram. Int.* **2018**, *44*, 6201–6211. [CrossRef]

40. Hassan, S.M.; Ahmed, A.I.; Mannaa, M.A. Preparation and characterization of SnO$_2$ doped TiO$_2$ nanoparticles: Effect of phase changes on the photocatalytic and catalytic activity. *J. Sci. Adv. Mater. Dev.* **2019**, *4*, 400–412. [CrossRef]

41. Yang, J.; Zhang, J.; Zou, B.; Zhang, H.; Wang, J.; Schubert, U.; Rui, Y. Black SnO$_2$-TiO$_2$ Nanocomposites with High Dispersion for Photocatalytic and Photovoltalic Applications. *ACS Appl. Nano Mater.* **2020**, *3*, 4265–4273. [CrossRef]

42. Lin, C.; Gao, Y.; Zhang, J.; Xue, D.; Fang, H.; Tian, J.; Zhou, C.; Zhang, C.; Li, Y.; Li, H. GO/TiO$_2$ composites as a highly active photocatalyst for the degradation of methyl orange. *J. Mater. Res.* **2020**, *35*, 1307–1315. [CrossRef]

43. Akti, F.; Balci, S. Synthesis of APTES and alcohol modified Sn/SBA-15 in presence of competitive ion: Test in degradation of Remazol Yellow. *Mater. Res. Bull.* **2022**, *145*, 111496. [CrossRef]

44. Soni, S.S.; Henderson, M.J.; Bardeau, J.F.; Gibaud, A. Visible-light photocatalysis in titania-based mesoporous thin films. *Adv. Mater.* **2008**, *20*, 1493–1498. [CrossRef]

45. Liao, Y.; Huang, C.; Liao, C.; Wu, J.; Wu, K. Synthesis of mesoporous titania thin films (MTTFs) with two different structures as photocatalysts for generating hydrogen from water splitting. *Appl. Energ.* **2012**, *100*, 75–80. [CrossRef]

46. Li, L.; Yan, J.; Wang, T.; Zhao, Z.-J.; Zhang, J.; Gong, J.; Guan, N. Sub-10 nm rutile titanium dioxide nanoparticles for efficient visible-light-driven photocatalytic hydrogen production. *Nat. Commun.* **2015**, *6*, 5881. [CrossRef]

47. Wang, Q.; Rhimi, B.; Wang, H.; Wang, C. Efficient photocatalytic degradation of gaseous toluene over F-doped TiO$_2$/exfoliated bentonite. *Appl. Surf. Sci.* **2020**, *530*, 147286. [CrossRef]

48. Preeti; Mishra, S.; Chakinala, N.; Chakinala, A.G. Bimetallic Bi/Zn decorated hydrothermally synthesized TiO$_2$ for efficient photocatalytic degradation of nitrobenzene. *Catal. Commun.* **2022**, *172*, 106538. [CrossRef]

49. Yan, B.; Chen, G.; Ma, B.; Guo, Y.; Zha, Y.; Li, J.; Wang, S.; Liu, J.; Zhao, B.; Xie, H. Construction of surface plasmonic Bi nanoparticles and α-Bi$_2$O$_3$ co-modified TiO$_2$ nanotube arrays for enhanced photocatalytic degradation of ciprofloxacin: Performance, DFT calculation and mechanism. *Sep. Purif. Technol.* **2024**, *330*, 125180. [CrossRef]

50. Bagwasi, S.; Tian, B.; Zhang, J.; Nasir, M. Synthesis, characterization and application of bismuth and boron Co-doped TiO$_2$: A visible light active photocatalyst. *Chem. Eng. J.* **2013**, *217*, 108–118. [CrossRef]

51. Huy, T.H.; Phata, B.D.; Kang, F.; Wang, Y.F.; Liu, S.H.; Thi, C.M.; You, S.J.; Chang, G.M.; Pham, V.V. SnO$_2$/TiO$_2$ nanotube heterojunction: The first investigation of NO degradation by visible light-driven photocatalysis. *Chemosphere* **2019**, *215*, 323–332. [CrossRef] [PubMed]

52. Shi, H.; Zhu, H.; Jin, T.; Chen, L.; Zhang, J.; Qiao, K.; Chen, Z. Construction of Bi/Polyoxometalate doped TiO$_2$ composite with efficient visible-light photocatalytic performance: Mechanism insight, degradation pathway and toxicity evaluation. *Appl. Surf. Sci.* **2023**, *615*, 156310. [CrossRef]

53. Li, G.; Li, J.; Li, G.; Jiang, G. N and Ti^{3+} co-doped 3D anatase TiO$_2$ superstructures composed of ultrathin nanosheets with enhanced visible light photocatalytic activity. *J. Mater. Chem. A* **2015**, *3*, 22073. [CrossRef]

54. Li, Y.; Feng, Y.; Bai, H.; Liu, J.; Hu, D.; Fan, J.; Shen, H. Enhanced visible-light photocatalytic performance of black TiO_2/SnO_2 nanoparticles. *J. Alloy. Compd.* **2023**, *960*, 170672. [CrossRef]

55. Song, Y.; Long, A.; Ge, X.; Bao, Z.; Meng, M.; Hu, S.; Gu, Y. Construction of floatable flower-like plasmonic Bi/BiOCl-loaded hollow kapok fiber photocatalyst for efficient degradation of RhB and antibiotics. *Chemosphere* **2023**, *343*, 140240. [CrossRef]

56. Li, J.; Jin, Z.; Zhang, Y.; Liu, D.; Ma, A.; Sun, Y.; Li, X.; Cai, Q.; Gui, J. Ag-induced anatase-rutile TiO_2-x heterojunction facilitating the photogenerated carrier separation in visible-light irradiation. *J. Alloy. Compd.* **2022**, *909*, 164815. [CrossRef]

57. Li, H.; Qiu, L.; Bharti, B.; Dai, F.; Zhu, M.; Ouyang, F.; Lin, L. Efficient photocatalytic degradation of acrylonitrile by Sulfur-Bismuth co-doped F-TiO_2/SiO_2 nanopowder. *Chemosphere* **2020**, *249*, 126135. [CrossRef]

58. Choukaife, A.E.; Aljerf, L. A descriptive study-in vitro: New validated method for checking Hap and Fap Behaviours. *Int. Med. J.* **2017**, *24*, 394–397.

59. Donohue, M.D.; Aranovich, G.L. A new classification of isotherms for Gibbs adsorption of gases on solids. *Fluid Phase Equilibr.* **1999**, *158–160*, 557–563. [CrossRef]

60. Liu, G.; Yang, H.G.; Wang, X.; Cheng, L.; Lu, H.; Wang, L.; Lu, G.; Cheng, H.M. Enhanced Photoactivity of Oxygen-Deficient Anatase TiO_2 Sheets with Dominant {001} Facets. *J. Phys. Chem. C* **2009**, *113*, 21784–21788. [CrossRef]

61. Lin, Z.; Orlov, A.; Lambert, R.M.; Payne, M.C. New insights into the origin of visible light photocatalytic activity of nitrogen-doped and oxygen-deficient anatase TiO_2. *J. Phys. Chem. B* **2005**, *109*, 20948–20952. [CrossRef] [PubMed]

62. Law, M.; Greene, L.E.; Radenovic, A.; Kuykendall, T.; Liphardt, J.; Yang, P. ZnO-Al_2O_3 and ZnO-TiO_2 core-shell nanowire dye-sensitized solar cells. *J. Phys. Chem. B* **2006**, *110*, 22652–22663. [CrossRef] [PubMed]

63. Parayil, S.K.; Kibombo, H.S.; Wu, C.; Peng, R.; Baltrusaitis, J.; Koodali, R.T. Enhanced photocatalytic water splitting activity of carbon-modified TiO_2 composite materials synthesized by a green synthetic approach. *Int. J. Hydrogen Energ.* **2012**, *37*, 8257–8267. [CrossRef]

64. Wang, X.; Yu, J.C.; Liu, P.; Wang, X.; Su, W.; Fu, X. Probing of photocatalytic surface sites on SO_4^{2-}/TiO_2 solid acids by in situ FT-IR spectroscopy and pyridine adsorption. *J. Photochem. Photobiol. A* **2006**, *179*, 339–347. [CrossRef]

65. Hong, W.; Li, C.; Tang, T.; Xu, H.; Yu, Y.; Liu, G.; Wang, F.; Lie, C.; Zhu, H. The photocatalytic activity of the $SnO_2/TiO_2/PVDF$ composite membrane in rhodamine B degradation. *New J. Chem.* **2021**, *45*, 2631–2642. [CrossRef]

66. Jiang, H.; Wang, R.; Li, Y.; Hong, X.; Liang, B. Glucose-tailored $SnO_2/TiO_2/RGO$ ternary composite for degradation of organic pollutants. *J. Phys. Chem. Solids* **2022**, *161*, 110442. [CrossRef]

67. Stefan, M.; Leostean, C.; Pana, O.; Popa, A.; Toloman, D.; Macavei, S.; Perhaita, I.; Barbu-Tudoran, L.; Silipas, D. Interface tailoring of SnO_2-TiO_2 photocatalysts modified with anionic/cationic surfactants. *J. Mater. Sci.* **2019**, *55*, 3279–3298. [CrossRef]

68. Wang, Q.; Fang, Y.; Meng, H.; Wu, W.; Chu, G.; Zou, H.; Cheng, D.; Chen, J. Enhanced simulated sunlight induced photocatalytic activity by pomegranate-like S doped $SnO_2@TiO_2$ spheres. *Colloids Surf. A* **2015**, *482*, 529–535. [CrossRef]

69. Shi, H.; Zhou, M.; Song, D.; Pan, X.; Fu, J.; Zhou, J.; Ma, S.; Wang, T. Highly porous SnO_2/TiO_2 electrospun nanofibers with high photocatalytic activities. *Ceram. Int.* **2014**, *40*, 10383–10393. [CrossRef]

70. Gao, Q.; Wu, X.; Fan, Y.; Zhou, X. Low temperature fabrication of nanoflower arrays of rutile TiO_2 on mica particles with enhanced photocatalytic activity. *J. Alloys Compd.* **2013**, *579*, 322–329. [CrossRef]

71. Chen, Y.; Jiang, Y.; Chen, B.; Tang, H.; Li, L.; Ding, Y.; Duan, H.; Wu, D. Insights into the enhanced photocatalytic activity of O-g-C_3N_4 coupled with SnO_2 composites under visible light irradiation. *J. Alloys Compd.* **2022**, *903*, 163739. [CrossRef]

72. Ma, H.; Wang, Y.; Zhang, Z.; Liu, J.; Yu, Y.; Zuo, S.; Li, B. A superior ternary Z-scheme photocatalyst of Bi/Black Phosphorus nanosheets/P-doped BiOCl containing interfacial P–P bond and metallic mediator for H_2O_2 production and RhB degradation. *Chemosphere* **2023**, *330*, 138717. [CrossRef] [PubMed]

73. Chen, Z.; Yu, S.; Liu, J.; Zhang, Y.; Wang, Y.; Yu, J.; Yuan, M.; Zhang, P.; Liu, W.; Zhang, J. C, F co-doping Ag/TiO_2 with visible light photocatalytic performance toward degrading Rhodamine B. *Environ. Res.* **2023**, *232*, 116311. [CrossRef] [PubMed]

74. Chen, Y.; Li, A.; Fu, X.; Peng, Z. Novel F-doped carbon nanotube@(N,F)-co-doped $TiO_{2-\delta}$ nanocomposite: Highly active visible-light-driven photocatalysts for water decontamination. *Appl. Surf. Sci.* **2023**, *609*, 155460. [CrossRef]

75. Khandekar, D.C.; Bhattacharyya, A.R.; Bandyopadhyaya, R. Role of impregnated nano-photocatalyst ($Sn_xTi_{(1-x)}O_2$) inside mesoporous silica (SBA-15) for degradation of organic pollutant (Rhodamine B) under UV light. *J. Environ. Chem. Eng.* **2019**, *7*, 103433. [CrossRef]

76. Wu, Y.M.; Xing, M.Y.; Tian, B.Z.; Zhang, J.L.; Chen, F. Preparation of nitrogen and fluorine co-doped mesoporous TiO_2 microsphere and photodegradation of acid orange 7 under visible light. *Chem. Eng. J.* **2010**, *162*, 710–717. [CrossRef]

77. Yang, G.D.; Jiang, Z.; Shi, H.H.; Jones, M.O.; Xiao, T.C.; Edwards, P.P.; Yan, Z.F. Study on the photocatalysis of F-S co-doped TiO_2 prepared using solvothermal method. *Appl. Catal. B Environ.* **2010**, *96*, 458–465. [CrossRef]